Geophysical Journal International

Geophys. J. Int. (2014) **199,** 1662–1676 doi: 10.1093/gji/ggu260

GJI Geomagnetism, rock magnetism and palaeomagnetism

Variational data assimilation for a forced, inertia-free magnetohydrodynamic dynamo model

Kuan Li,[1] Andrew Jackson[1] and Philip W. Livermore[2]

[1]*Institute of Geophysics, ETH Zurich, Zurich* 8092, *Switzerland. E-mail: kuan.li@erdw.ethz.ch*

[2]*School of Earth and Environment, University of Leeds, Leeds LS*2 9*JT, UK*

Accepted 2014 July 4. Received 2014 July 4; in original form 2014 January 31

SUMMARY

Variational data assimilation (4DVar) is a powerful technique for tuning dynamic models to observations, in order not only to forecast future time evolution of the system, but to make inferences about quantities that are otherwise unconstrained by observation. We apply this technique, well-grounded in meteorology and oceanography, to the Earth's core where incompressible fluid motions in an electrically conducting medium are responsible for magnetic field generation. Our dynamic model's momentum equation neglects inertia such that the entire evolution depends only on the structure of the initial magnetic field; time evolution of the system is solely governed by the equation of magnetic induction. Nevertheless the dynamic system encompasses the effects of rotation, Lorentz forces and viscosity and aims to mimic a reasonable force-balance in the Earth's core. Building on the work of Li *et al.*, in order to optimize the data-fit subject to the dynamics, we further develop the mathematical structure of the adjoint equations of the system. We address the feasibility of recovering 3-D spatial properties of the system using only time-varying 2-D observations of different character. Using closed-loop testing, we demonstrate the retrievability of the initial state (and thus the entire trajectory) of the system over convective timescales, when sampling in regions in which magnetic induction dominates over diffusion. The results suggest the possibility of retrieving the entire trajectory of the dynamo system of the Earth using the 400-yr model of secular variation *gufm1*.

Key words: Numerical solutions; Numerical approximations and analysis; Probabilistic forecasting; Dynamo: theories and simulations; Geomagnetic induction; Planetary interiors.

1 INTRODUCTION

Earth's magnetic field is generated by fluid motions in its electrically conducting liquid outer core, whereby convective motions are thought to be driven by cooling of the Earth and crystallization of the solid inner core (Olson 2007). This system is governed by a set of three coupled equations that describe the conservation of momentum, energy and the evolution in time of the spatially varying magnetic field. The resulting magnetic field permeates the silicate mantle and is observable at the Earth's surface, thus providing a window into the dynamics of the core (Jackson & Finlay 2007).

Beginning with the pioneering work of Glatzmaier & Roberts (1995) and Kageyama & Sato (1995), 3-D self-consistent numerical models that simulate this physical system have been instrumental in demonstrating the feasibility of this picture of dynamo action in the core. The computer codes that simulate this dynamic system have now reached a level of maturity such that, additionally, various basic features of the field are reproduced well: for example, dipolarity and field strength. Successes of these models are pre-dominantly measured statistically, by way of the degree to which features appear, on average, to agree with long-term features of the palaeomagnetic field, or with statistical features of the 400-yr record of the observed field from the model *gufm1* (Jackson *et al.* 2000). Recently, even the temporal characteristics of the numerical models, the secular variation, have been statistically compared to observations with considerable success (Christensen *et al.* 2012). Whilst the ultimate aim of such activities is to characterize and to understand the force balances and physical structures within the core, another approach is to analyse the system's observed time evolution deterministically rather than statistically. In this context, properties of the model, such as, *inter alia*, the dipole moment are analysed in time. The evolution of such a quantity is termed a trajectory and the purpose of this work is to tune the predicted trajectories of the physical model (with the proviso that time span not be too long) to be in accord with observations.

The techniques used to tune such a physical model to a set of observations are known as 'data assimilation', and have been used with great success in the last few decades in meteorology (Lynch 2008) and oceanography (Ghil 1989). The particular

approach we adopt is termed 'variational data assimilation' and builds upon our previous work in this area (Li *et al.* 2011).

Data assimilation as applied to geomagnetism is a relatively nascent activity, beginning with the work of Fournier *et al.* (2007), Sun *et al.* (2007) and Liu *et al.* (2007), part of a broad body of applications to the geosciences, which includes seismology (Tarantola 1984). In meteorology, oceanography and geomagnetism, two flavours of data assimilation have been adopted, namely sequential and variational data assimilation (Evensen 2006; Talagrand 2010); the former has recently contributed to the International Geomagnetic Reference Field (IGRF; see Kuang *et al.* 2010). Although both techniques can be shown to be equivalent in a certain limit (Evensen 2006), our choice of the variational method is motivated both by mathematical succinctness, efficiency and its ease of computability.

The power of data assimilation is both in its ability to produce forecasts of the dynamic model, but also to make inferences in quantities that are otherwise hidden from observation. One ultimate aim of this activity is to produce a predictive tool for the internal magnetic field, with a wide variety of applications in industry and space-weather (Siscoe & Solomon 2006). A second but much broader goal is to use the tuned dynamic models to constrain quantities such as the present-day internal magnetic field inside the core and the mechanism which controls its time evolution (Fournier *et al.* 2010).

Observations of the Earth's magnetic field over the last few hundred years exist in the form of data from permanent magnetic observatories, shipping logs, land surveys (Jonkers *et al.* 2003) and satellites (Olsen *et al.* 2009); on longer timescales archeomagnetic data supplements the record (Korte *et al.* 2005; Donadini *et al.* 2009). The surface measurements are typically transformed into a spherical harmonic model describing the potential field at the Earth's surface. Assuming that the mantle is an electrical insulator, we can straightforwardly downward continue the magnetic field to the edge of the dynamo region, the core–mantle boundary (CMB), providing a known distribution of the poloidal magnetic field over the spherical surface. We term these observations time-varying 2-D observations, which differ substantially from those used in meteorology because of their limited spatial distribution. Although these data constrain only the surface of the dynamic system and not within, the equivalent 2-D problem in meteorology has been found to have encouraging results (Compo *et al.* 2006). The de facto model of time-varying magnetic field over the last 400 yr is *gufm1* of Jackson *et al.* (2000), which provides a convenient parametrized representation of the observations and can be used for assimilation. In the future, however, it is envisaged that data assimilation techniques should be constrained by the original observations directly. One further difference between the meteorological and geomagnetic observations is that the latter are confined to only large scale features. This band-limited nature takes the form, in the spherical harmonic domain, of a truncation to degrees less than approximately 15 (Langel & Estes 1982). Nevertheless, 400 yr of continuous data represents several core-turnover times (of about 150 yr) and thus, by analogy with the atmosphere, gives reason to believe that the data are sufficient to constrain a large part of the interior dynamics of the core.

Data assimilation techniques have already been used successfully in geomagnetism, but in far more focussed problems. For example, Canet *et al.* (2009) applied a variational data assimilation scheme to a magnetohydrodynamic (MHD) system specialized for short-term dynamics (decadal timescales), the so-called quasi-geostrophic (QG) system. The QG model is a simplified system based on the assumption that the flow is nearly invariant in the direction parallel to the axis of Earth's rotation, due to the strong Coriolis force. The resulting 2-D flow interacts with the radial component of the magnetic field at the CMB, whose signature can be observed. In a subsequent landmark work, Gillet *et al.* (2010) were able, for the first time, to constrain the interior geomagnetic profile, and its intensity over much of the core to be 2–3 mT.

At the heart of data assimilation is the prescription of the dynamic model. In this work, we choose an inertia-free version of the Navier–Stokes equations coupled with the magnetic induction equation. We consider two variants, one system that is driven by a prescribed time-invariant radial force, and a second decaying system. This inertia-free system is motivated by the smallness of the Rossby number in the core, and follows the original philosophy of Glatzmaier & Roberts (1995). In concert with other authors, our system includes viscosity despite the fact that it is generally considered negligible in the core. This approximation is unavoidable for numerical reasons. In this formulation, the velocity at every point in time is uniquely determined by both the prescribed radial force and Lorentz force. The advantage of this simplification is that the initial structure of the magnetic field determines the entire evolution of the system. Our prescribed radial force reduces the loss of energy; in the future it is envisaged that a time-varying buoyancy force will be included whose initial structure will then also be an unknown.

At this point we briefly summarize the mathematical developments that are intrinsic to the 4DVar scheme. Given the aim of bringing the model predictions into accord with observations, we define a chi-squared measure of misfit between these two quantities that we then seek to minimize. The minimization is achieved by the derivation of the so-called adjoint system of equations, which operate in reverse time. A series of backward and forward integrations in time, over the prescribed time window, gives access to the gradient of the misfit with respect to the initial condition (I.C.) that is sought. This gradient is used, in conjunction with a conjugate gradient or Newton-type method (Nocedal & Wright 2006), to iteratively update the current estimate of the I.C. until convergence is achieved. A computational scheme is designed around a spectral discretization of the equations, based on spherical harmonics and an expedient radial representation for the full sphere geometry as described in Li *et al.* (2011); this is the topic of Sections 3 and 4 of the paper. In Sections 5 and 6, we describe closed-loop tests, in which the ability to retrieve known I.C.s is quantified under different observational scenarios. We discuss the results and their implications for forecasting and inference of geophysical properties in Earth's core in Section 7.

2 THE GOVERNING EQUATIONS OF EARTH's DYNAMO SYSTEM

The geodynamo system is governed by three coupled equations for the velocity field $\mathbf{u}^*$, magnetic field $\mathbf{B}^*$ and temperature anomaly T^*, where the symbol * represents dimensional fields. The flow is assumed incompressible and vanishes at the CMB. The Earth's mantle is a weak electrical conductor compared with the Earth's core, hence we consider the mantle as an electrical insulator and the magnetic field satisfies an insulating boundary condition (B.C.) at the CMB. The geodynamo system can be written as

$$\frac{\partial \mathbf{u}^*}{\partial t} + (\mathbf{u}^* \cdot \nabla)\mathbf{u}^* + 2\Omega^* \times \mathbf{u}^* = -\frac{1}{\rho}\nabla p + \frac{1}{\rho}\mathbf{J}^* \times \mathbf{B}^* + \nu\nabla^2\mathbf{u}^* + \alpha g T^* \hat{\mathbf{r}}, \quad (1)$$

$$\frac{\partial \mathbf{B}^*}{\partial t} = \nabla \times (\mathbf{u}^* \times \mathbf{B}^*) + \eta \nabla^2 \mathbf{B}^*, \tag{2}$$

$$\frac{\partial T^*}{\partial t} + \mathbf{u}^* \cdot \nabla T^* = \kappa \nabla^2 T^* + h^*, \tag{3}$$

$$\nabla \cdot \mathbf{u}^* = \nabla \cdot \mathbf{B}^* = 0,$$

where $\mathbf{J}^* = \frac{1}{\mu_0} \nabla \times \mathbf{B}^*$ is the electrical current density, ρ is the mass density of the core, ν is the kinematic viscosity, Ω^* is the angular velocity, η is the magnetic diffusivity, κ is the thermal-diffusivity, g is the gravitational acceleration, α is the thermal expansion coefficient, $\alpha g T^* \hat{\mathbf{r}}$ is the buoyancy force and h^* is an internal energy source. In this work, we neglect (3) and replace the buoyancy force by a prescribed forcing.

2.1 Simplified MHD model and the control parameters

We work in the full sphere and follow Glatzmaier & Roberts (1995), non-dimensionalizing the dynamo system (1–2) using the characteristic length R (the radius of Earth's core) and the magnetic decay time R^2/η. With the removal of the temperature equation (3) from the dynamo system, we replace the buoyancy force by a static force, $\mathcal{F}$, in the radial direction. Our governing equations now read

$$E_m \left[\frac{\partial \mathbf{u}}{\partial t} + \mathbf{u} \cdot \nabla \mathbf{u} \right] + \hat{\mathbf{z}} \times \mathbf{u} = -\nabla \pi + (\nabla \times \mathbf{B}) \times \mathbf{B} + E_k \nabla^2 \mathbf{u} + \mathcal{F},$$

$$\frac{\partial \mathbf{B}}{\partial t} = \nabla \times (\mathbf{u} \times \mathbf{B}) + \nabla^2 \mathbf{B}, \tag{4}$$

where the dimensional fields $\mathbf{u}^*$ and $\mathbf{B}^*$ are rescaled by the factors $\frac{R}{\eta}$ and $(2\Omega^* \mu_0 \rho \eta)^{-1/2}$ such that $\mathbf{u} = \frac{R}{\eta}\mathbf{u}^*$ and $\mathbf{B} = (2\Omega^* \mu_0 \rho \eta)^{-1/2} \mathbf{B}^*$. Two small parameters appear in these equations, the magnetic Ekman number (sometimes called the magnetic Rossby number), E_m, which is estimated to be 10^{-9} in Earth's core and the Ekman number, E_k, estimated to be 10^{-15}. Following Glatzmaier & Roberts (1995), we neglect the inertial term but retain viscosity for numerical reasons. This simplification filters out numerous types of wave motion, such as Alfvén, torsional and Rossby waves, but remains a good description of the dynamics over centennial and longer timescales. We note that a similar conclusion concerning the neglect of the inertial force is reached from a kinematic analysis: taking the westward drift rate of 5×10^{-4} m s^{-1}, gives a conventional Rossby number of 10^{-6}. A consequence of this approximation is that the Navier–Stokes equation is converted from prognostic (predictive) to diagnostic form, that is, at every instant in time, $\mathbf{u}$ is enslaved to $\mathcal{F}$ and the magnetic field through the Lorentz force. The governing equations now read

$$\mathcal{N}(\mathbf{u}, \mathbf{B}) \equiv \hat{\mathbf{z}} \times \mathbf{u} + \nabla \pi - (\nabla \times \mathbf{B}) \times \mathbf{B} - E_k \nabla^2 \mathbf{u} - \mathcal{F} = 0, \tag{5}$$

$$\mathcal{I}(\mathbf{u}, \mathbf{B}) \equiv \frac{\partial \mathbf{B}}{\partial t} - \nabla \times (\mathbf{u} \times \mathbf{B}) - \nabla^2 \mathbf{B} = 0. \tag{6}$$

An estimate of the ratio of magnetic induction to diffusion is the magnetic Reynolds number, R_m, which in our rescaled system, we take to be simply $R_m = \widehat{u}$, where

$$\widehat{u} = \sqrt{\frac{1}{V} \int_V \mathbf{u}^2 \mathrm{d}V} = \sqrt{\frac{\langle \mathbf{u}, \mathbf{u} \rangle}{V}}, \tag{7}$$

denotes a volumetric rms and V is the volume of the sphere. In this paper, we will also use the volume integral notation $\langle \, , \rangle$

$$\langle a, b \rangle = \int_V a \, b \, \mathrm{d}V \tag{8}$$

for arbitrary quantities a and b. As we show later in the paper, in general this estimate differs from the true ratio of the magnitudes of the induction to diffusion terms, since it does not take into account their full spatial structure. In our study, we also use the horizontal rms as a function of radius, that is the horizontal rms of $\mathbf{B}$ can be written as

$$\overline{\mathbf{B}} = \sqrt{\int_\Omega \frac{1}{4\pi} \mathbf{B}^2 \sin\theta \mathrm{d}\theta \mathrm{d}\phi}, \tag{9}$$

where Ω is the spherical surface, not to be confused with the same symbol used for Earth's angular velocity in (1).

Taking the estimated Earth value for the magnetic diffusivity $\eta = 1.5$ m^2 s^{-1} (Olson 2007), we have a time unit of the MHD system of (6) of $R^2/\eta = 2 \times 10^5$ yr. Similarly, the Elsasser unit of field strength is $(2\Omega^* \mu_0 \rho \eta)^{-1/2} \approx 0.6$ mT. Adoption of the new values for η of de Koker *et al.* (2012) would alter those scales by factors of 3 and $\sqrt{3}$, respectively, but this has not been done. We choose a moderate Ekman number, $E_k = 10^{-4}$, such that the viscous force is small compared to the Coriolis force and large enough to make the model computationally feasible. If the rotation rate of the model is one day as that for Earth, one has the viscous diffusivity of the order of 10^5 times larger than the magnetic diffusivity, where as in Earth, this value is expected to be 10^5 times smaller. The solution of (5 and 6) is uniquely determined by the I.C. of the magnetic field $\mathbf{B}(t = 0) = \mathbf{B}_0$ and the boundary conditions (B.C.s) for $\mathbf{B}$ and $\mathbf{u}$, which are chosen as electrical insulating B.C. for $\mathbf{B}$ and a non-slip B.C. for $\mathbf{u}$. Note that the velocity field is diagnostically determined and its solution can be written as $\mathbf{u} = \mathbf{u}_B + \mathbf{u}_F$, where $\mathbf{u}_B$ (driven magnetically) and $\mathbf{u}_F$ (driven by $\mathcal{F}$) satisfy the linear equations

$$\hat{\mathbf{z}} \times \mathbf{u}_B - E_k \nabla^2 \mathbf{u}_B + \nabla \pi_1 = (\nabla \times \mathbf{B}) \times \mathbf{B},$$

$$\hat{\mathbf{z}} \times \mathbf{u}_F - E_k \nabla^2 \mathbf{u}_F + \nabla \pi_2 = \mathcal{F}. \tag{10}$$

Let us briefly consider the energetics of the system (5) and (6). The total energy integrated over all space satisfies

$$\frac{\mathrm{d}}{\mathrm{d}t} \int \mathbf{B}^2 \, \mathrm{d}V = -\int (\nabla \times \mathbf{B})^2 \mathrm{d}V - E_k \int (\nabla \times \mathbf{u})^2 \mathrm{d}V + \int \mathcal{F} \cdot \mathbf{u} \, \mathrm{d}V. \tag{11}$$

For $\mathcal{F} = 0$, the magnetic field, therefore, decays at least as fast as it would do under free decay, that is when $\mathbf{u} = 0$. In order to reduce the rapid decay of the energy, a static driving force is introduced, $\mathcal{F}$, that provides a positive rate of working on the system at the initial time for a given I.C., $\mathbf{B}_0$, that is $\int \mathcal{F} \cdot \mathbf{u} \, \mathrm{d}V > 0$ at $t = 0$. We note that both of $\mathbf{B}$ and $\mathbf{u}$ are dynamically varying and hence there is no guarantee of the positivity of $\int \mathcal{F} \cdot \mathbf{u} \, \mathrm{d}V$ for all time; $\mathcal{F}$ is fully described in Section 5.2.

3 4DVAR AND THE ADJOINT DYNAMO MODEL

Using the technique developed in Li *et al.* (2011), we define a positive definite quantity termed the misfit, χ^2, which measures the

deviation between the predictions and the observations

$$\chi^2 = \frac{1}{2}\int_{t=0}^{\tau} \langle \mathcal{O}(\mathbf{B}) - y, \mathcal{O}(\mathbf{B}) - y\rangle \mathrm{d}t + \frac{1}{2}\int_{t=0}^{\tau} \langle \mathcal{O}_u(\mathbf{u}) - y_u, \mathcal{O}_u(\mathbf{u}) - y_u\rangle \mathrm{d}t, \quad (12)$$

where $[0, \tau]$ is the observation time window, $\langle , \rangle$ is defined in (8), and continuous observations in time are considered presently. As a thought experiment, we consider the possibility of observations of both magnetic and velocity fields, and consequently define observation operators $\mathcal{O}$ and $\mathcal{O}_u$ (see Section 4.2), which generate the predictions $\mathcal{O}(\mathbf{B})$ and $\mathcal{O}_u(\mathbf{u})$ at the same positions in space and time as the measurements $y(\mathbf{r}, t)$ and $y_u(\mathbf{r}, t)$, respectively. We look for the optimal trajectory satisfying the governing equations (5) and (6) and best fitting the observations. Hence χ^2 in (12) has to be further constrained by (5) and (6) and written as

$$\chi^2 = \frac{1}{2}\int_{t=0}^{\tau} \langle \mathcal{O}(\mathbf{B}) - y, \mathcal{O}(\mathbf{B}) - y\rangle \mathrm{d}t + \frac{1}{2}\int_{t=0}^{\tau} \langle \mathcal{O}_u(\mathbf{u}) - y_u, \mathcal{O}_u(\mathbf{u}) - y_u\rangle \mathrm{d}t + \int_{t=0}^{\tau} \langle \mathbf{u}^\dagger, \mathcal{N}(\mathbf{u}, \mathbf{B})\rangle \mathrm{d}t + \int_{t=0}^{\tau} \langle \mathbf{B}^\dagger, \mathcal{I}(\mathbf{u}, \mathbf{B})\rangle \mathrm{d}t + \int_{t=0}^{\tau} \left[\langle p_1^\dagger, \nabla\cdot\mathbf{u}\rangle + \langle p_2^\dagger, \nabla\cdot\mathbf{B}\rangle\right] \mathrm{d}t, \quad (13)$$

where $\mathbf{u}^\dagger$ and $\mathbf{B}^\dagger$ are Lagrange multipliers (also known as adjoint variables), $\mathcal{N}$ and $\mathcal{I}$ are defined in (5 and 6), and the adjoint pressure terms $p_1^\dagger$ and $p_2^\dagger$ are required to implement the divergence free conditions for $\mathbf{u}$ and $\mathbf{B}$, and are a necessary part of the numerical method which we use to project the vector fields onto a divergence-free discretization. For details, please refer to Li *et al.* (2011).

We minimize χ^2 in (13) by computing the downhill direction of χ^2 with respect to $\mathbf{B}_0$. The downhill direction can be written as

$$\nabla_{\mathbf{B}_0}\chi^2 = -\mathbf{B}_0^\dagger, \quad (14)$$

where the adjoint variables $\mathbf{B}^\dagger$ and $\mathbf{u}^\dagger$ satisfy the adjoint system,

$$\mathbf{u}^\dagger \times \hat{\mathbf{z}} - E_k\nabla^2\mathbf{u}^\dagger = -\nabla p_1^\dagger + \mathbf{B}\times(\nabla\times\mathbf{B}^\dagger) - O_u^\dagger[O_u\mathbf{u} - y_u], \quad (15)$$

$$-\frac{\partial\mathbf{B}^\dagger}{\partial t} = (\nabla\times\mathbf{B}^\dagger)\times\mathbf{u} - \nabla p_2^\dagger + \left[\nabla\times(\mathbf{B}\times\mathbf{u}^\dagger) + \mathbf{u}^\dagger\times(\nabla\times\mathbf{B})\right] + \left[\nabla^2\right]^\dagger\mathbf{B}^\dagger - O^\dagger[O\mathbf{B} - y]. \quad (16)$$

$[\nabla^2]^\dagger$ is the adjoint operator of ∇^2; we construct the discrete version as the transpose of the appropriate matrix as we did in Li *et al.* (2011).[1]

$\mathbf{B}^\dagger$ at the terminal time satisfies the terminal condition $\mathbf{B}_\tau^\dagger = 0$, $\mathbf{u}^\dagger$ and $\mathbf{B}^\dagger$ satisfy the same B.C.s as those of $\mathbf{u}$ and $\mathbf{B}$, respectively and the adjoint pressure terms $p_1^\dagger$ and $p_2^\dagger$ satisfy

$$\nabla^2 p_1^\dagger = \nabla\cdot\left[-\mathbf{u}^\dagger\times\hat{\mathbf{z}} + \mathbf{B}\times(\nabla\times\mathbf{B}^\dagger)\right], \quad (17)$$

$$\nabla^2 p_2^\dagger = \nabla\cdot\left[(\nabla\times\mathbf{B}^\dagger)\times\mathbf{u} + \mathbf{u}^\dagger\times(\nabla\times\mathbf{B})\right], \quad (18)$$

[1] The statement concerning the self-adjointness of the Laplace operator acting on a magnetic field with insulating B.C.s as in Li *et al.* (2011) is only correct when the integration volume is all space, which was not the case in the study of Li *et al.* (2011); thus the statement is erroneous.

where the B.C. on $p_2^\dagger$ is $p_2^\dagger = 0$ at $r = 1$. Similar to the pressure term, π, in (5), the term $p_1^\dagger$ is treated by the discretization method in Section 4, and does not enter the solution of the system (see eq. 26). The adjoint system is driven by the deviation between the predictions and the observations, propagates backwards in time from $t = \tau$ to $t = 0$ and the solution $\mathbf{B}^\dagger$ at $t = 0$ is the downhill direction of the misfit with respect to the unknown $\mathbf{B}_0$. Also note that the solution of the adjoint Navier–Stokes equation in (15) is diagnostic and depends entirely on the given forcing term $\mathbf{B}\times(\nabla\times\mathbf{B}^\dagger)$, in a similar way to the Navier–Stokes equation itself in (5). The radial force is invariant in time and hence does not appear in the adjoint system.

4 NUMERICAL DISCRETIZATION OF THE FORWARD AND THE ADJOINT DYNAMO MODEL

4.1 Numerical discretizations

We use a poloidal–toroidal representation for the divergence-free fields, $\mathbf{u}$ and $\mathbf{B}$. Each poloidal and toroidal scalar is further expanded in fully normalized spherical harmonics Y_l^m in colatitude and longitude (θ, ϕ) with associated radial basis functions. We design the radial basis functions for the poloidal and toroidal scalars such that the bases are orthonormal under volumetric integration and satisfy insulating B.C. on $\mathbf{B}$ and no-slip B.C. on $\mathbf{u}$; these can be written as

$$\mathbf{B} = \mathbf{B}_S + \mathbf{B}_T = \sum_{(n,l,m)} a_{(n,l,m)}\mathbf{S}_{(n,l,m)} + b_{(n,l,m)}\mathbf{T}_{(n,l,m)}, \quad (19)$$

$$\mathbf{u} = \mathbf{u}_S + \mathbf{u}_T = \sum_{(n,l,m)} c_{(n,l,m)}\mathbf{s}_{(n,l,m)} + d_{(n,l,m)}\mathbf{t}_{(n,l,m)}, \quad (20)$$

where $a_{(n,l,m)}$ and $b_{(n,l,m)}$ are the poloidal and toroidal coefficients for the magnetic field, $c_{(n,l,m)}$ and $d_{(n,l,m)}$ are the poloidal and toroidal coefficients for the flow and the vector basis functions $\mathbf{S}_{(n,l,m)}$, $\mathbf{T}_{(n,l,m)}$, $\mathbf{s}_{(n,l,m)}$ and $\mathbf{t}_{(n,l,m)}$ can be further written as

$$\mathbf{S}_{(n,l,m)} = \nabla\times\nabla\times(\Phi_n^l(r)Y_l^m\hat{\mathbf{r}}) \quad \text{and} \quad \mathbf{T}_{(n,l,m)} = \nabla\times(\Psi_n^l(r)Y_l^m\hat{\mathbf{r}}),$$
$$\mathbf{s}_{(n,l,m)} = \nabla\times\nabla\times(Z_n^l(r)Y_l^m\hat{\mathbf{r}}) \quad \text{and} \quad \mathbf{t}_{(n,l,m)} = \nabla\times(\Psi_n^l(r)Y_l^m\hat{\mathbf{r}}). \quad (21)$$

The orthogonality of the vector basis functions can be written as (Li *et al.* 2011)

$$\langle \mathbf{S}_{(n,l,m)}, \mathbf{S}_{(n',l',m')}\rangle = \delta_{l,l'}\delta_{m,m'}l(l+1) \times \int_{r=0}^{1}\left[\frac{l(l+1)}{r^2}\Phi_n^l\Phi_{n'}^{l'} + \frac{\partial\Phi_n^l}{\partial r}\frac{\partial\Phi_{n'}^{l'}}{\partial r}\right]\mathrm{d}r = \delta_{n,n'}\delta_{l,l'}\delta_{m,m'},$$

$$\langle \mathbf{T}_{(n,l,m)}, \mathbf{T}_{(n',l',m')}\rangle = \delta_{l,l'}\delta_{m,m'}l(l+1) \times \int_{r=0}^{1}\Psi_n^l\Psi_{n'}^{l'}dr = \delta_{n,n'}\delta_{l,l'}\delta_{m,m'},$$

$$\langle \mathbf{S}_{(n,l,m)}, \mathbf{T}_{(n',l',m')}\rangle = 0, \quad (22)$$

with similar relations for $\mathbf{s}_{(n,l,m)}$ and $\mathbf{t}_{(n,l,m)}$. All of our radial basis functions, based on one-sided Jacobi polynomials (Boyd 2001; Livermore 2010), are regular at the origin and infinitely differentiable everywhere. Our specially constructed radial basis functions $\Phi_n^l(r)$, $\Psi_n^l(r)$ satisfy the B.C. (Bullard & Gellman 1954)

$$\mathrm{d}\Phi_n^l/\mathrm{d}r + l\Phi_n^l = 0 \text{ at } r = 1, \qquad \Psi_n^l = 0 \text{ at } r = 1, \quad (23)$$

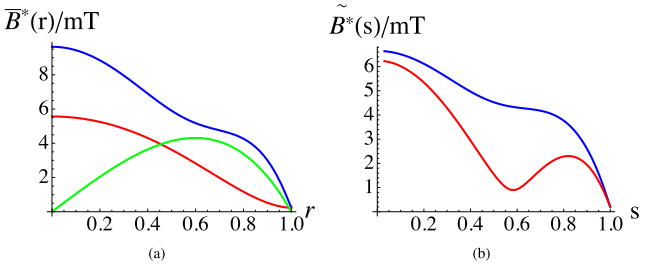

Figure 1. (a) The internal structure of $\mathbf{B}^*$ shown by the horizontal rms of: (i) the total field $\overline{\mathbf{B}}^*$ shown in blue, (ii) the radial field $\overline{B}_r^*$ shown in red and (iii) the toroidal component of field $\overline{\mathbf{B}}_T^*$ shown in green. (b) The rms of $\mathbf{B}^*$ shown in blue and B_s^* shown in red, where $\widetilde{\mathbf{B}}$ denotes the rms over a cylinder of cylindrical radius s.

Table 1. The poloidal and toroidal coefficients of the magnetic profile shown in Fig. 1, $\mathbf{a}_{(n,l,m)}$ and $\mathbf{b}_{(n,l,m)}$, written in non-dimensional units and rounded to *two* decimal places.

$a_{(1,1,0)} = -2.03$	$a_{(2,1,0)} = 2.80$	$b_{(1,1,0)} = 3.46$
$a_{(1,1,1/c)} = -0.13$	$a_{(2,1,1/c)} = 0.17$	$b_{(1,1,1/c)} = 0.22$
$a_{(1,1,1/s)} = 0.37$	$a_{(2,1,1/s)} = -0.51$	$b_{(1,1,1/s)} = 0.63$
$a_{(1,2,0)} = -0.39$	$a_{(2,2,0)} = 0.54$	$b_{(1,2,0)} = 0.67$
$a_{(1,2,1/c)} = 0.55$	$a_{(2,2,1/c)} = -0.76$	$b_{(1,2,1/s)} = 0.94$
$a_{(1,2,1/s)} = -0.42$	$a_{(2,2,1/s)} = 0.57$	$b_{(1,2,1/s)} = 0.70$
$a_{(1,2,2/c)} = 0.31$	$a_{(2,2,2/c)} = -0.42$	$b_{(1,2,2/c)} = 0.52$
$a_{(1,2,2/s)} = -0.07$	$a_{(2,2,2/s)} = 0.09$	$b_{(1,2,2/s)} = 0.12$

and Z_n^l (the radial basis for the poloidal part of the flow) satisfies the no-slip B.C.

$$Z_n^l = 0 \quad \text{and} \quad \frac{\mathrm{d}}{\mathrm{d}r} Z_n^l = 0 \quad \text{at} \quad r = 1. \tag{24}$$

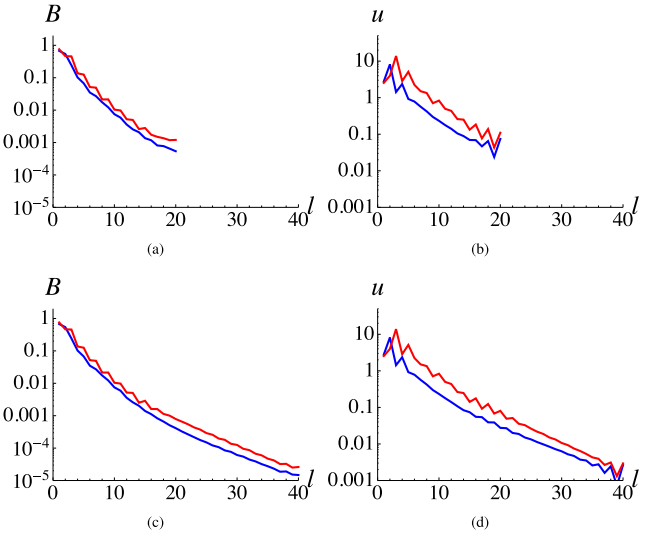

Figure 3. The spectral convergence of $\mathbf{B}$ and $\mathbf{u}$ as a function of spherical harmonic degree l at the terminal time $t = \tau$ for different resolutions $N_{\max} = L_{\max} = 20$ in (a) and (b) and $N_{\max} = L_{\max} = 40$ in (c) and (d), where $\tau = 1/40$ (5000 yr) and the blue and red curves show the poloidal and toroidal contribution.

We truncate our spectral expansions at degree and order $L_{\max}$, and in radius, the radial index n, at $N_{\max}$. More details of the numerical scheme can be found in Livermore *et al.* (in preparation).

We derive the adjoint system in a Hilbert space using the volume integral within the sphere as the inner product and we discretize the spatial part of the MHD system (5) and (6) and its adjoint (15) and (16) using the orthonormal basis functions (21) in the same

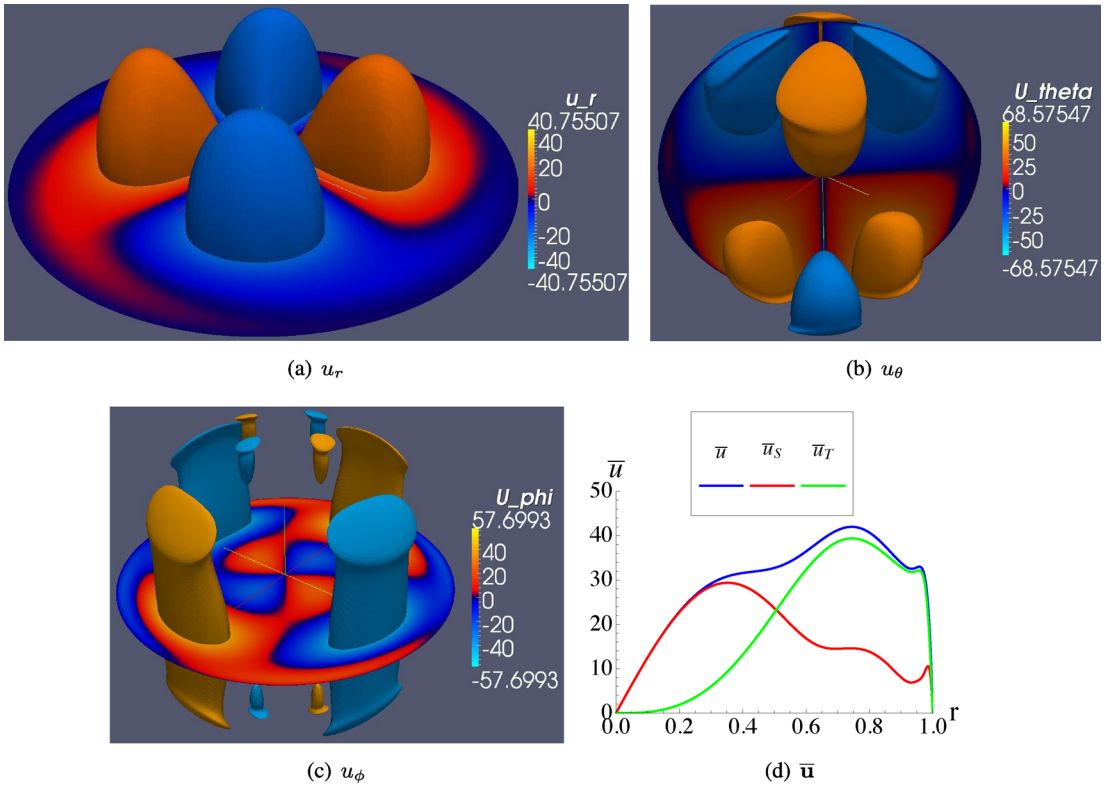

Figure 2. Plots of the iso-surface of the static convection pattern driven by the radial force, $\mathcal{F}$, for the r, θ and ϕ components in (a), (b) and (c) and the horizontal rms of the velocity as a function of radius in (d), where the red, green and blue curves are for the poloidal, toroidal and the total field.

Hilbert space. Hence, as we proved in Li *et al.* (2011), the adjoint of the discrete system is identical to the discretized continuous adjoint system.

The spatial part of the induction equation and its adjoint is discretized and solved using the pseudo-spectral method developed in Li *et al.* (2011). For the Navier–Stokes equation and its adjoint we pre-compute the matrix representation $M_{i,j}$ of the operator L, where $L(\mathbf{u}_i) = \hat{\mathbf{z}} \times \mathbf{u}_i - E_k \nabla^2 \mathbf{u}_i + \nabla \pi_i$, that is

$$M_{i,j} = \langle \mathbf{u}_j, L(\mathbf{u}_i) \rangle = \langle \mathbf{u}_j, \hat{\mathbf{z}} \times \mathbf{u}_i \rangle - E_k \langle \mathbf{u}_j, \nabla^2 \mathbf{u}_i \rangle + \langle \mathbf{u}_j, \nabla \pi_i \rangle$$
$$= \langle \mathbf{u}_j, \hat{\mathbf{z}} \times \mathbf{u}_i \rangle - E_k \langle \mathbf{u}_j, \nabla^2 \mathbf{u}_i \rangle, \tag{25}$$

where $\langle , \rangle$ is the volume integral defined in (8), i and j are the collective indies of (n, l, m), $\mathbf{u}_i$ are the basis functions describing $\mathbf{u}$ defined in (21) and π_i is the pressure force associated with $\mathbf{u}_i$. To be clear, the subscript i refers to the ith (3-D) vector basis function describing the flow, and not to a component in the ith direction of some coordinate system. To see that the pressure term does not contribute to the discretized system, we note that when every member of the basis represents a non-penetrable flow at the CMB ($u_r = 0$ at $r = 1$), we have

$$\int_V \mathbf{u}_i \cdot \nabla \pi_i = \int_V \nabla \cdot (\pi_i \mathbf{u}_i) - \pi_i \nabla \cdot \mathbf{u}_i \, \mathrm{d}V$$
$$= \int_\Omega \pi_i \, [\mathbf{u}_i \cdot \hat{\mathbf{r}}] \, \mathrm{d}\Omega = 0, \tag{26}$$

where $\mathrm{d}\Omega$ is the surface element, $\mathrm{d}\Omega = r^2 \sin\theta \mathrm{d}\theta \mathrm{d}\phi$. Having the discretized operator, $M_{i,j}$ in hand, the matrix representation of the adjoint operator $L^\dagger$ reads $M^\dagger_{i,j} = M_{j,i}$ (Li *et al.* 2011). The solution of the Navier–Stokes equation and its adjoint can be written as

$$\mathbf{u} = \begin{pmatrix} \mathbf{c} \\ \mathbf{d} \end{pmatrix} = M^{-1} [\langle \mathbf{u}_i, (\nabla \times \mathbf{B}) \times \mathbf{B} + \mathcal{F} \rangle]^T, \tag{27}$$

$$\mathbf{u}^\dagger = \begin{pmatrix} \mathbf{c}^\dagger \\ \mathbf{d}^\dagger \end{pmatrix} = [M^\dagger]^{-1} [\langle \mathbf{u}_i, \mathbf{B} \times (\nabla \times \mathbf{B}^\dagger) - O_u^\dagger [O_u(\mathbf{u}) - y_u] \rangle]^T, \tag{28}$$

where $[\mathbf{c}, \mathbf{d}]^T$ and $[\mathbf{c}^\dagger, \mathbf{d}^\dagger]^T$ are the spectral coefficients of the velocity field and its adjoint, defined by (21).

Using the symmetry of the operator L in the Navier–Stokes equation, one can substantially reduce the computational complexity for computing (27) and (28). L is an even operator (Zhang 1991) in (5), which decouples $\mathbf{u}$ into even and odd symmetries, and is a symmetric operator in the azimuthal wave number, m, which decouples all m modes. Therefore $M_{i,j}$ can be divided into $2L_{\max} + 2$ square diagonal blocks and each one can be inverted independently.

We evolve the MHD system (5) and (6) forwards in time using an Euler scheme for the initial time step and an Adams–Bashforth second order scheme for the following time steps.

Having the downhill direction (14) in hand, the minimization of the misfit is carried out using a limited memory quasi-Newton method (L-BFGS), where the second derivative of χ^2, known as Hessian, is estimated and gradually improved in the minimization step. The numerical algorithm is based on Nocedal (1980).[2]

We choose the model resolution K to be $K = N_{\max} = L_{\max}$ that leads to $4K^2(K+1)$ coefficients that describe each of the forward and adjoint models. Since the computational complexity scales as K^4 (Li *et al.* 2010), we solve the MHD system (5) and (6) and its adjoint (15) and (16) numerically in parallel using the Message Passing Interface (MPI), where (i) the magnetic induction equation and its adjoint are parallelized in radius and (ii) linear solvers defined in (27) and (28) are parallelized by symmetry class. The minimization step is computed on a single processor using the L-BFGS package, where at each assimilation cycle, the misfit and the downhill direction, χ^2 and $\mathbf{B}_0^\dagger$, are collected from each processor.

[2] The software package is acquired from http://users.eecs.northwestern.edu/nocedal/lbfgs.html

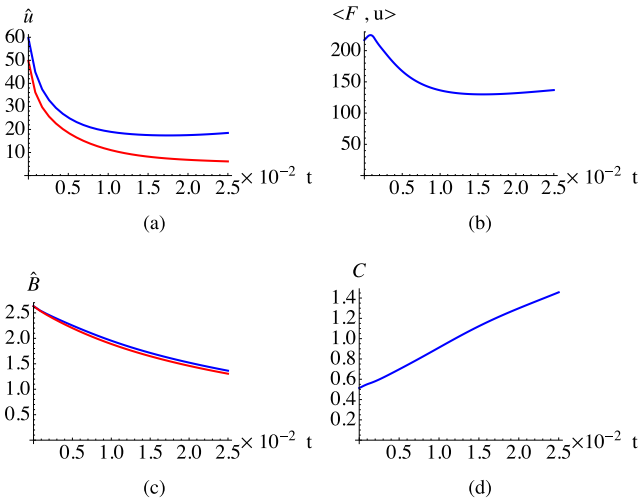

Figure 4. Plots of several quantities within the simulation time window $\tau = 1/40$ (5000 yr): (a) The volume rms of the velocity field with and without $\mathcal{F}$ in blue and red, respectively. (b) The rate of working of the driving force, $\mathcal{F}$. (c) The volume rms of $\mathbf{B}$ with and without $\mathcal{F}$ in blue and red, respectively. (d) The ratio C of the volume rms values of the driving force and the Lorentz force.

4.2 The observations and the misfit

Let $\mathcal{O}$ be the observation operator that measures, at a certain radius, the degree l and order m spherical harmonic components of the radial part of the modelled magnetic field $\mathbf{B}$. The aim of our assimilation is to fit the $\mathcal{O}(\mathbf{B}(t_i))$ to the corresponding datum at time t_i, denoted y_i (Li *et al.* 2011).

In our discrete system, the misfit can be written as

$$\chi^2_{\mathbf{B}} = \frac{1}{2} \sum_i [\mathcal{O}(\mathbf{B}(t_i)) - y_i]^T \cdot [\mathcal{O}(\mathbf{B}(t_i)) - y_i], \tag{29}$$

where $\mathcal{O}(\mathbf{B}(t_i))$ and y_i, vectors of spherical harmonic coefficients, are truncated at degree L_{ob}.

Similarly, we define the observation operators $\mathcal{O}_{Su}$ and $\mathcal{O}_{Tu}$ that measure the 3-D structure of the poloidal and toroidal flow, respectively. The contribution of the flow at radius r_j to the misfit reads

$$\chi^2_u = \chi^2_{Su} + \chi^2_{Tu} = \frac{1}{2} \sum_i \int_{r=r_j} [\mathbf{u}(t_i) - \mathbf{u}_{\mathrm{ob}}(t_i)]^2 \, \mathrm{d}\Omega, \tag{30}$$

where $\mathbf{u}_{\mathrm{ob}}$ is the observed flow at time t_i. Although our equations are formulated for continuous observations, in our discretized system we observe at discrete points in time, t_i, at uniform spacing of $\Delta\tau$ throughout the time window $[0, \tau]$.

5 THE CHARACTERISTICS OF THE FORWARD MODEL

Before studying the retrievability of the initial magnetic field in the closed-loop experiments, we first describe the evolution of the forward model itself.

5.1 The I.C. for magnetic field

The entire trajectory of (5) and (6) is uniquely determined by both the initial structure of the magnetic field and the B.C.s. Although the magnetic field internal to the Earth's core is unknown, here we create a synthetic magnetic profile of maximum degree $l = 2$ that has been constructed to honour various constraints, in that (i) its radial component B_r matches the *gufm1* model at 1990 at the CMB and (ii) the horizontal rms of B_r is 4.6 mT at $r = 7/20$ (Buffett *et al.* 2002). Fig. 1(a) illustrates the profile of various components of magnetic field as a function of radius r and Fig. 1(b) the magnetic profile of various components as a function of cylindrical radius s. The corresponding spectral coefficients $a_{(n,l,m)}$ and $b_{(n,l,m)}$ are listed in Table 1. More details can be found in Appendix A.

5.2 The choice of body force

In some models in this study, we choose a radial driving force $\mathcal{F}$, which is large scale and of spherical harmonic degree 2 and order 2 (and with cosine phase) with an intensity comparable to the Lorentz force of the MHD system (5) and (6) (see Fig. 4d). We define $\mathcal{F}$ to be

$$\mathcal{F} = \frac{5}{2}\sqrt{429}r^3\left(9r^2 - 7\right)Y_2^{2/c}\hat{\mathbf{r}}, \tag{31}$$

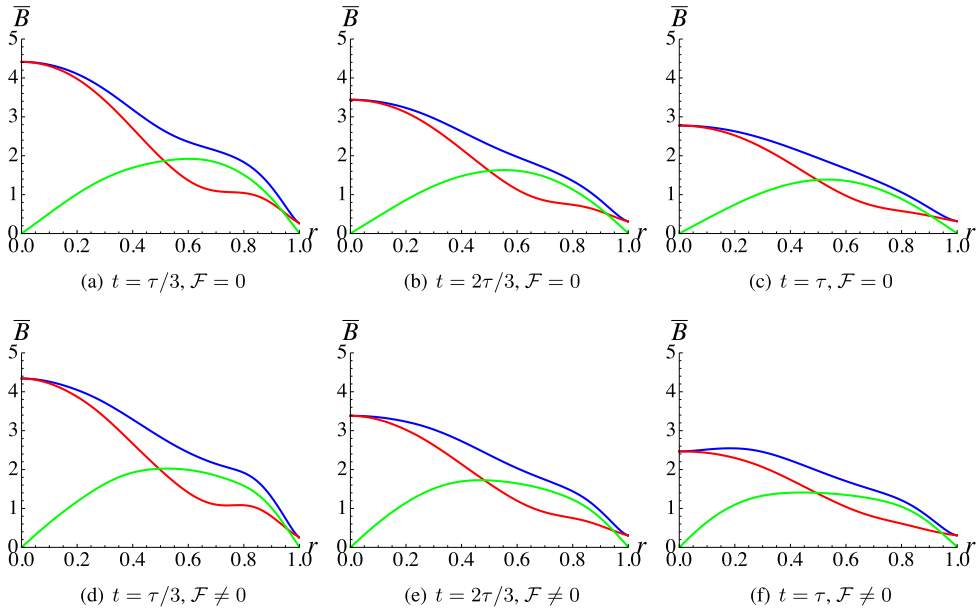

Figure 5. The horizontal rms of **B** as a function of r, where $\tau = 1/40$ (5000 yr), the total magnetic field, the poloidal part of the flow and toroidal part of the magnetic field, are shown in blue, red and green. Interestingly, for both cases with and without $\mathcal{F}$, the magnetic fields in the bulk decay exponentially in time in a similar fashion, however their intensities at the CMB vary much less (see Fig. 6).

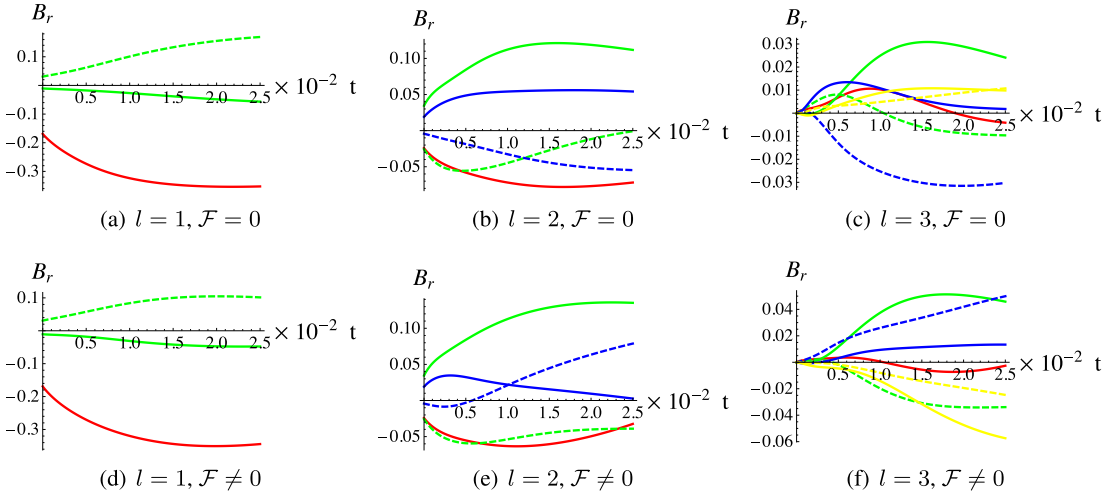

Figure 6. The trajectories of spherical harmonic components $l = 1$, 2 and 3 of B_r within the time window $[0, \tau]$ at the CMB, where $\tau = 1/40$ (5000 yr). The red, green, blue and yellow curves show the $m = 0$, 1, 2 and 3 components and the solid lines show the cosine phase and the dashed lines show the sine phase.

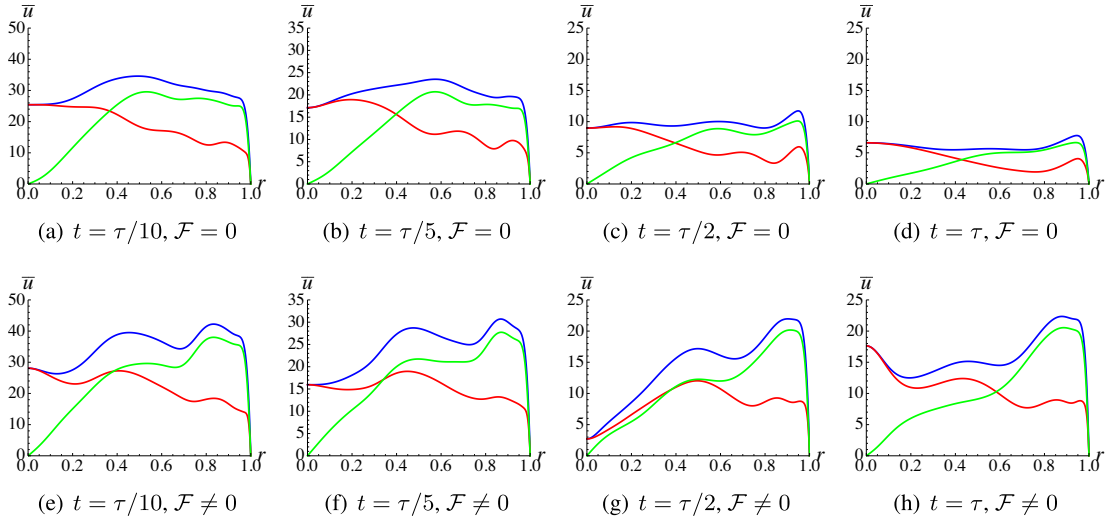

Figure 7. The horizontal rms of **u** as a function of r without (a–d) and with (e–h) the driving force, where $\tau = 1/40$ (5000 yr), the total flow, the poloidal part of the flow and toroidal part of the flow, are shown in blue, red and green. Of particular note is the Ekman layer close to the CMB, in which the flow decreases rapidly to zero.

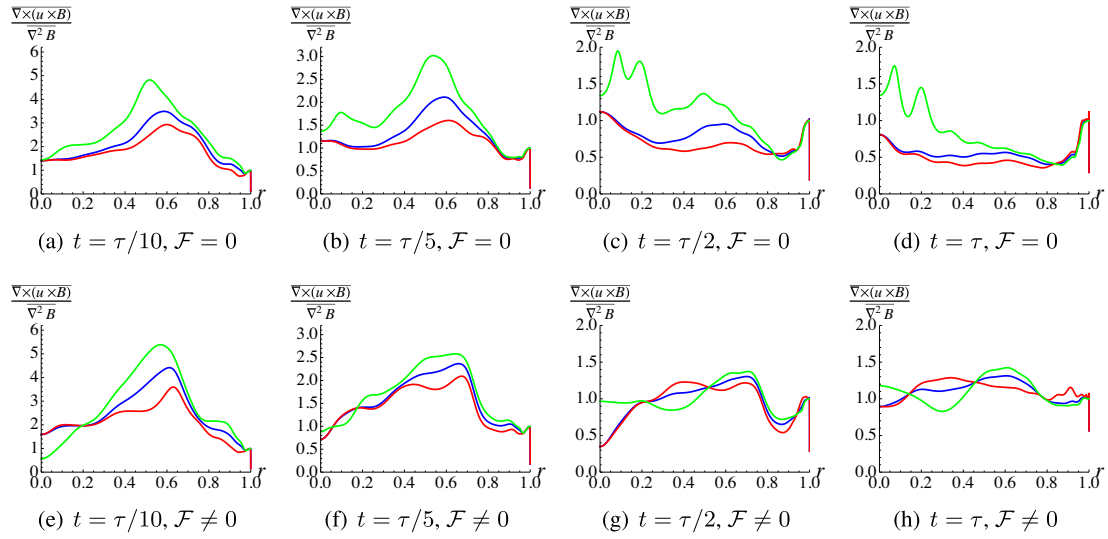

Figure 8. The ratio of the horizontal rms of the vectors describing magnetic induction and diffusion, as a function of r without (a–d) and with (e–h) the driving force at certain time snapshots, where $\tau = 1/40$ (5000 yr). Blue shows this ratio calculated using the total vectors, red and green show the ratio calculated using only the poloidal and toroidal components of the vectors, respectively.

Table 2. Summary of observational scenarios considered. $\mathbf{B}_0^{(0)}$ is the initial guess of the I.C., τ is the assimilation time window, $\Delta\tau$ is the time interval between two observations, χ_0^2 and χ_N^2 are the misfits at the initial and the final iteration, respectively, D is the recovery performance defined in (35) at the final iteration and N is the number of iterations used. Note that the differences in χ_0^2 for Cases 3a and 3b originate in the fact that one has a forcing $\mathcal{F}$ and the other does not, thus leading to a different trajectory over which the misfit is calculated.

	$\mathcal{F}$	2-D observation	$\mathbf{B}_0^{(0)}$	τ	$\Delta\tau$	χ_0^2	χ_N^2	D	N
Case 1	$\mathcal{F} \neq 0$	$B_r\|_{r=1}$	$\mathbf{0}$	$\frac{1}{40}$	$\tau/500$	2.5×10^2	3.8×10^{-1}	1.03	302
Case 2	$\mathcal{F} = 0$	$B_r\|_{r=1}$ & $\mathbf{u}\|_{r=0.85}$	$\mathbf{0}$	$\frac{1}{40}$	$\tau/500$	1.1×10^6	3.4×10^2	0.11	375
Case 3a	$\mathcal{F} = 0$	$B_r\|_{r=1/2}$	$\mathbf{B}_0/2$	$\frac{1}{40}$	$\tau/500$	1.9×10^3	2.7×10^{-2}	0.22	354
Case 3b	$\mathcal{F} \neq 0$	$B_r\|_{r=1/2}$	$\mathbf{B}_0/2$	$\frac{1}{40}$	$\tau/500$	3.5×10^3	1.5×10^{-1}	0.17	163
Case 3c	$\mathcal{F} \neq 0$	$B_r\|_{r=1/2}$	$\mathbf{0}$	$\frac{1}{25}$	$\tau/1000$	1.2×10^4	2.7×10^{-1}	0.42	214

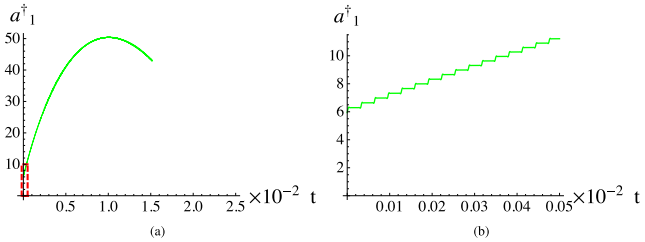

Figure 9. The trajectory of the poloidal (1, 1, 0) mode of the adjoint field $B^{\dagger}$ at the third iteration of the assimilation in Case 1, where in (a) the adjoint field $a_1^{\dagger}$ starts from zero at the terminal time, $t = \tau$ and backward propagates until $t = 0$ giving the required derivative; and (b) is a close-up of the red rectangular region in (a).

which has the property that

$$\int \mathcal{F} \cdot \mathbf{u} \, \mathrm{d}V > 0, \tag{32}$$

for the initial time $t = 0$ and can be further written as the combination of a poloidal field and a scalar potential field, that is

$$\mathcal{F} = (F, 0, 0) = -10\mathbf{S}_2^{2/c} + \nabla R_2^{2/c}, \tag{33}$$

where $\mathbf{S}_l^m$ is a poloidal vector basis function defined in (21) and the scalar potential term $R_2^{2/c}$ is

$$R_2^{2/c} = -\left[\frac{5}{8}\sqrt{429}r^2\left(7r^4 - 10r^2 + 3\right)Y_2^{2/c}\right]. \tag{34}$$

In the absence of magnetic field, this generates a static convection pattern, $\mathbf{u}_F$, defined in (10), well-mixing the magnetic field lines in the core.

Figs 2(a)–(c) illustrates the form of $\mathbf{u}_F$ in the r, θ and ϕ directions and Fig. 2(d) the horizontal rms of various components of the velocity.

Since the Ekman number is sufficiently small ($E_k = 10^{-4}$), in the outer half of the core, the flow $\mathbf{u}_F$ is largely geostrophic (see Fig. 2c) with an rms intensity of about 30 and a maximum of 40 (see Fig. 2d). Recall that this represents an approximate magnetic Reynolds number.

5.3 Model convergence

With the chosen Ekman number $E_k = 10^{-4}$ and the time window, $[0, \tau]$, where $\tau = 1/40$, our model is fully resolved using the spatial resolution $N_{\max} = L_{\max} = 20$. Given the strength of the flow, this time window is close to one convective overturn time. Fig. 3 illustrates the spectral convergence of the solution **B** for different

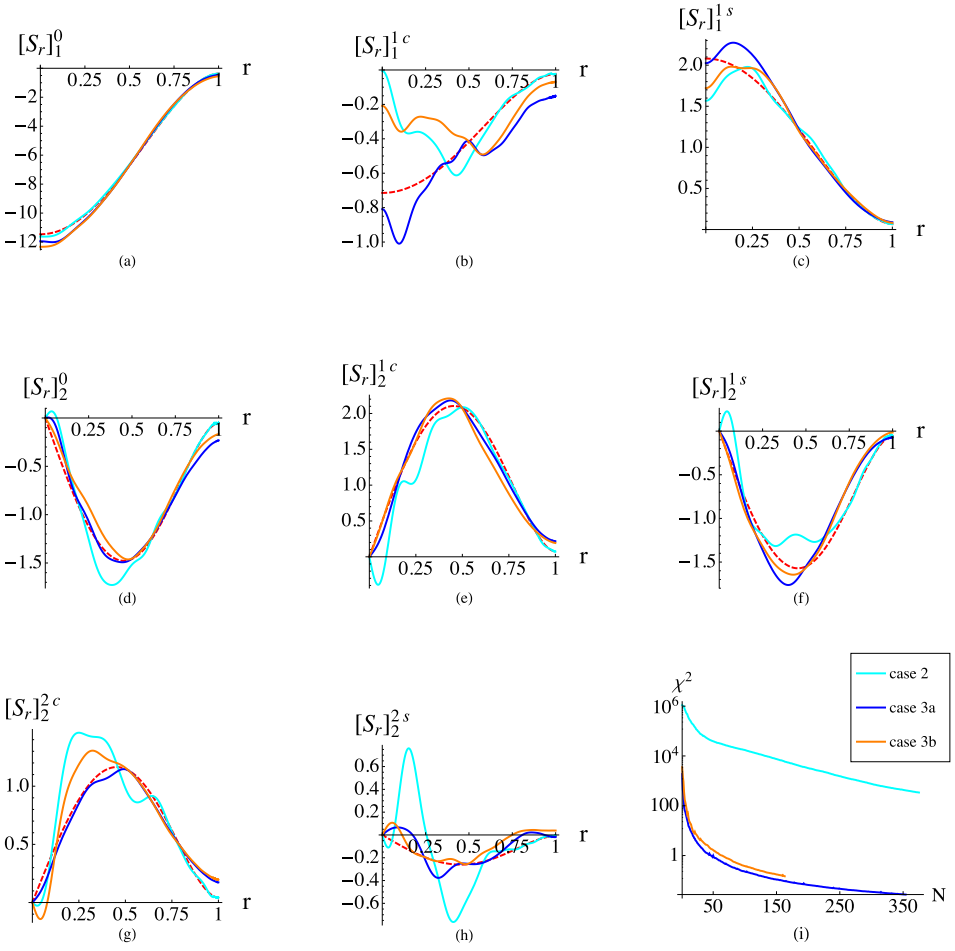

Figure 10. The poloidal part of the retrieved I.C. and the reduction of the misfit as a function of iteration for Cases 2, 3a and 3b at the final iteration of each one for each spherical harmonic degree, l, and order m, where the dashed red lines stand for the truth and the solid lines are for the retrieved components (see the legend for the colour correspondence to different cases).

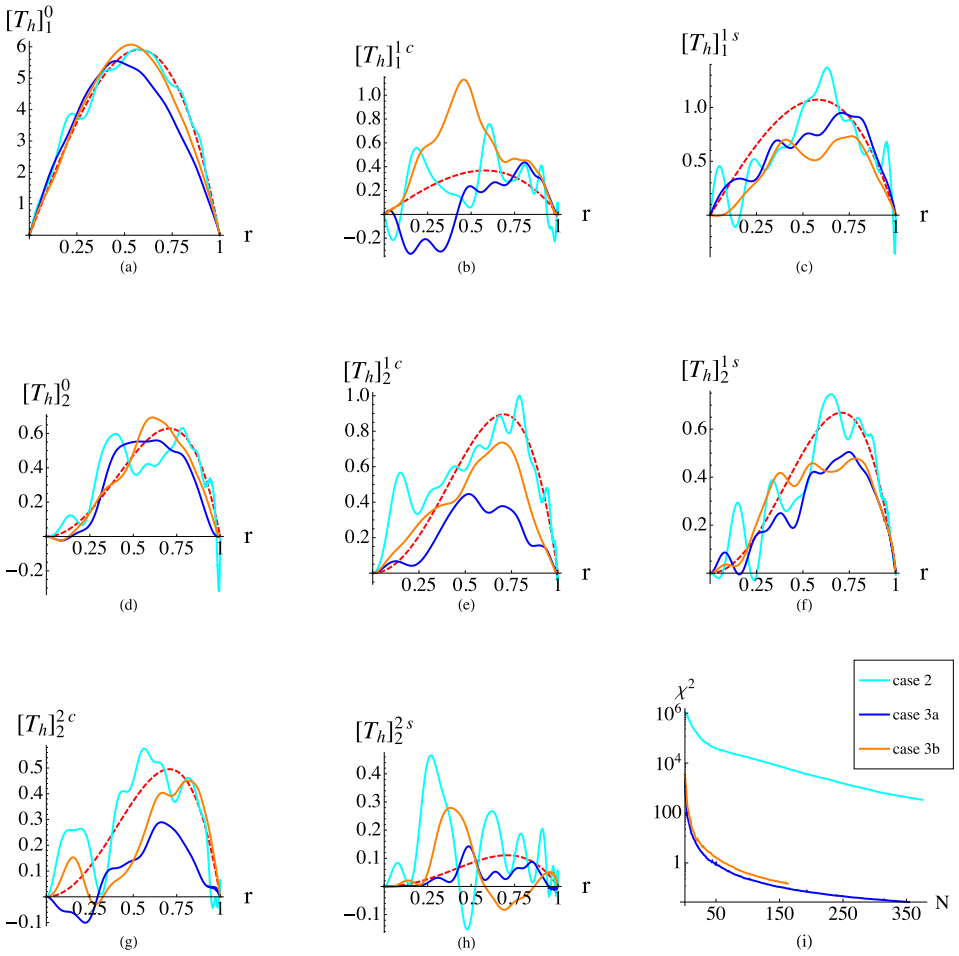

Figure 11. The toroidal part of the retrieved I.C. and the reduction of the misfit as a function of iteration for Cases 2, 3a and 3b at the final iteration of each one for each spherical harmonic degree, l, and order m, where the dashed red lines stand for the truth and the solid lines are for the retrieved components (see the legend for the colour correspondence to different cases).

spatial resolutions, $N_{\max} = L_{\max} = m_{\max} = 20$ (upper panel) and $N_{\max} = L_{\max} = m_{\max} = 40$ (lower panel). Clearly, the simulation with the spatial resolution of $N_{\max} = L_{\max} = m_{\max} = 20$ demonstrates exponential convergence and will be used for all subsequent studies; the optimal time step, Δt, determined empirically, is about $10^{-5.5}$.

5.4 The internal dynamics of the forward model

We now investigate the internal dynamics of the forward model, beginning with the role of the force $\mathcal{F}$. Fig. 4(a) shows the volume rms of the velocity field with and without $\mathcal{F}$, shown in blue and red curves. The volumetric rms of the flow varies between 10 and 60, similar to the typical value of the horizontal rms of 40 found above. Within this time window, $[0, \tau]$ ($\tau = 1/40$), the static driving force positively injects energy into the flow, that is $\int_V \mathcal{F} \cdot \mathbf{u}\, \mathrm{d}V > 0$ for $t \in [0, \tau]$ (see Fig. 4 b) and increases the flow intensity by about 20–30 per cent. However, this increase in flow strength does not greatly influence the energy evolution of the magnetic field and for both cases, the energy of the magnetic field decays in a similar fashion. Fig. 4(c) illustrates the volume rms of the magnetic field within the time window $[0, \tau]$ with and without $\mathcal{F}$ as shown in blue and red, respectively.

Fig. 5 illustrates the horizontal rms of $\mathbf{B}$ as a function of r and Fig. 6 shows B_r evaluated at the CMB. For both figures, the upper panels show the trajectories without the driving force and the lower panels show those with $\mathcal{F}$. We note that the magnetic field decays exponentially in a similar fashion in the bulk of the core (see Fig. 5), however its intensity at the CMB varies much less (see Fig. 6).

Fig. 7 illustrates the horizontal rms of the velocity field for models driven without and with $\mathcal{F}$. In both cases, the flow is strong in the bulk of the core and decreases rapidly to zero at the CMB in the Ekman boundary layer. Without driving, the intensity of the flow is more evenly distributed in radius in the bulk of the core than that with the driving force. When driving is present, the flow is stronger at the top of the core.

As will become apparent in the next section, when we try to retrieve the initial magnetic field structure, it will be important to consider the regions of the modelled core in which the process of magnetic induction dominates magnetic diffusion. Fig. 8 shows the ratio of the horizontal rms of these two quantities. Of particular note is the dominant influence of diffusion in the Ekman boundary layers in which the flow is weak (due to the imposed non-slip boundary), and the evolution of the magnetic field is entirely governed by

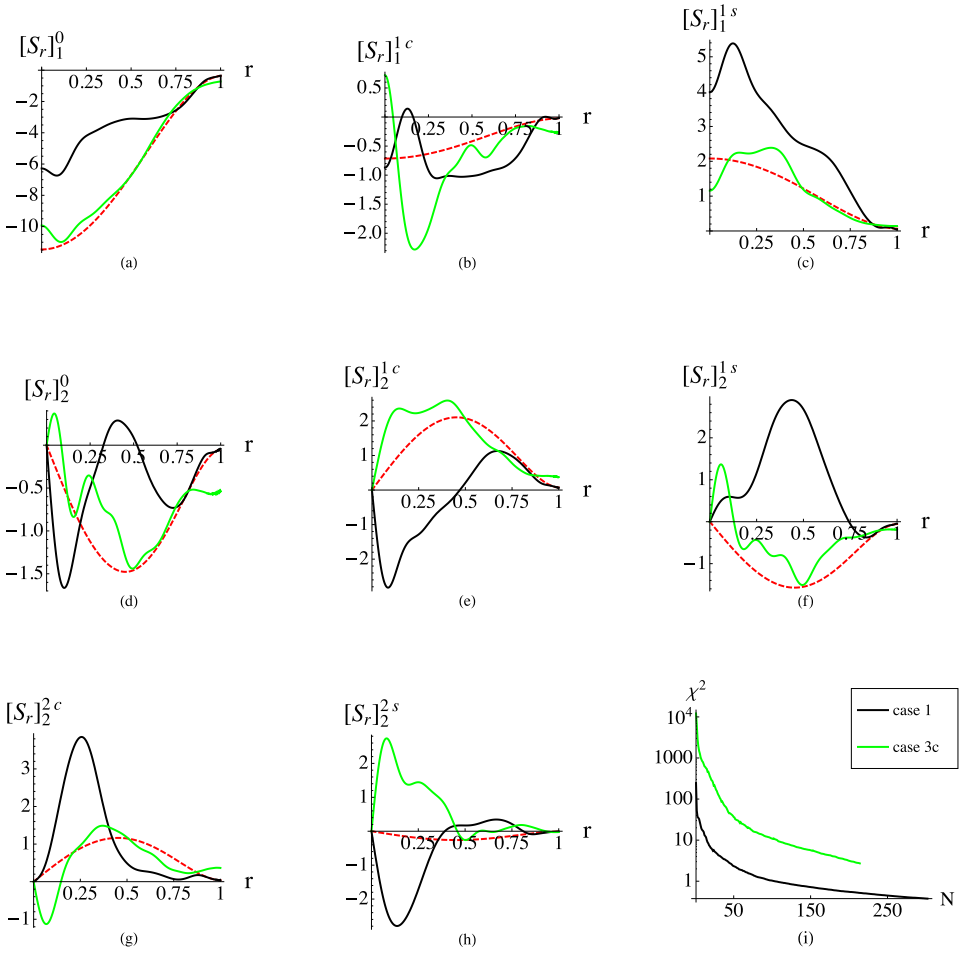

Figure 12. The poloidal part of the retrieved I.C. and the reduction of the misfit as a function of iteration for Cases 1 and 3c at the final iteration of each one for each spherical harmonic degree, l, and order m, where the dashed red lines stand for the truth and the solid lines are for the retrieved components (see the legend for the colour correspondence to different cases).

diffusion. Away from the CMB, the induction process gradually overwhelms the diffusion process and the ratio reaches a maximum in the bulk of the core. When driven by $\mathcal{F}$, we see in the figure, at each snapshot in time, that the ratio of induction to diffusion is generally higher than in those models without the driving force.

6 VARIATIONAL DATA ASSIMILATION

6.1 Closed-loop testing

In order to study the retrievability of the initial magnetic field, on which the entire trajectory of the system depends, we now discuss the setup of several closed-loop experiments. Using the magnetic profile given in Table 1 as the true I.C., we evolve and measure (to degree $L_{\max}$) the coupled system of the magnetic field and flow, at certain time snapshots and locations. These are then used as observational data in the variational data assimilation.

When setting up the closed-loop tests, there are various issues to consider: (i) the location of the observation, (ii) the specific quantity being observed, (iii) the frequency of observation and (iv) the length of the time window of the observations. All four points, in addition to the initial estimate of $\mathbf{B}_0$, have a bearing on the rate of iterative convergence and the retrieval accuracy. Therefore, we consider three classes of observational strategies, which are described below and summarzed in Table 2. For each case, we report the converged value of χ^2 along with quantity D, measuring within the 3-D volume the deviation from the true model, which, recall, is of spherical harmonic degrees, $l = 1$ and 2; a low value of D signifies an almost perfect model recovery, where

$$D = \frac{\widehat{\mathbf{B}_0 - \mathbf{B}_0^{(n)}}}{\widehat{\mathbf{B}_0}} \tag{35}$$

and $\mathbf{B}_0^{(n)}$ is the estimated I.C. at the nth iteration.

(i) Case 1: observing only B_r at the CMB.
Geomagnetic observations on the Earth's surface allow only inference of the field on the CMB. The simplest and most geophysically relevant strategy is therefore to observe on $r = 1$. We observe at 500 equally spaced snapshots, over the time window $\tau = 1/40$. We use the initial estimate for $\mathbf{B}_0$ of zero, which we loosely equate to having no knowledge of the solution regime.

(ii) Case 2: observing B_r at the CMB and $\mathbf{u}$ within and close to the top of the core.
We extend Case 1 by considering, as a thought experiment, inclusion of observations of $\mathbf{u}$, which will more fully constrain the nonlinear dynamics of the model. We choose to observe the flow at a radius

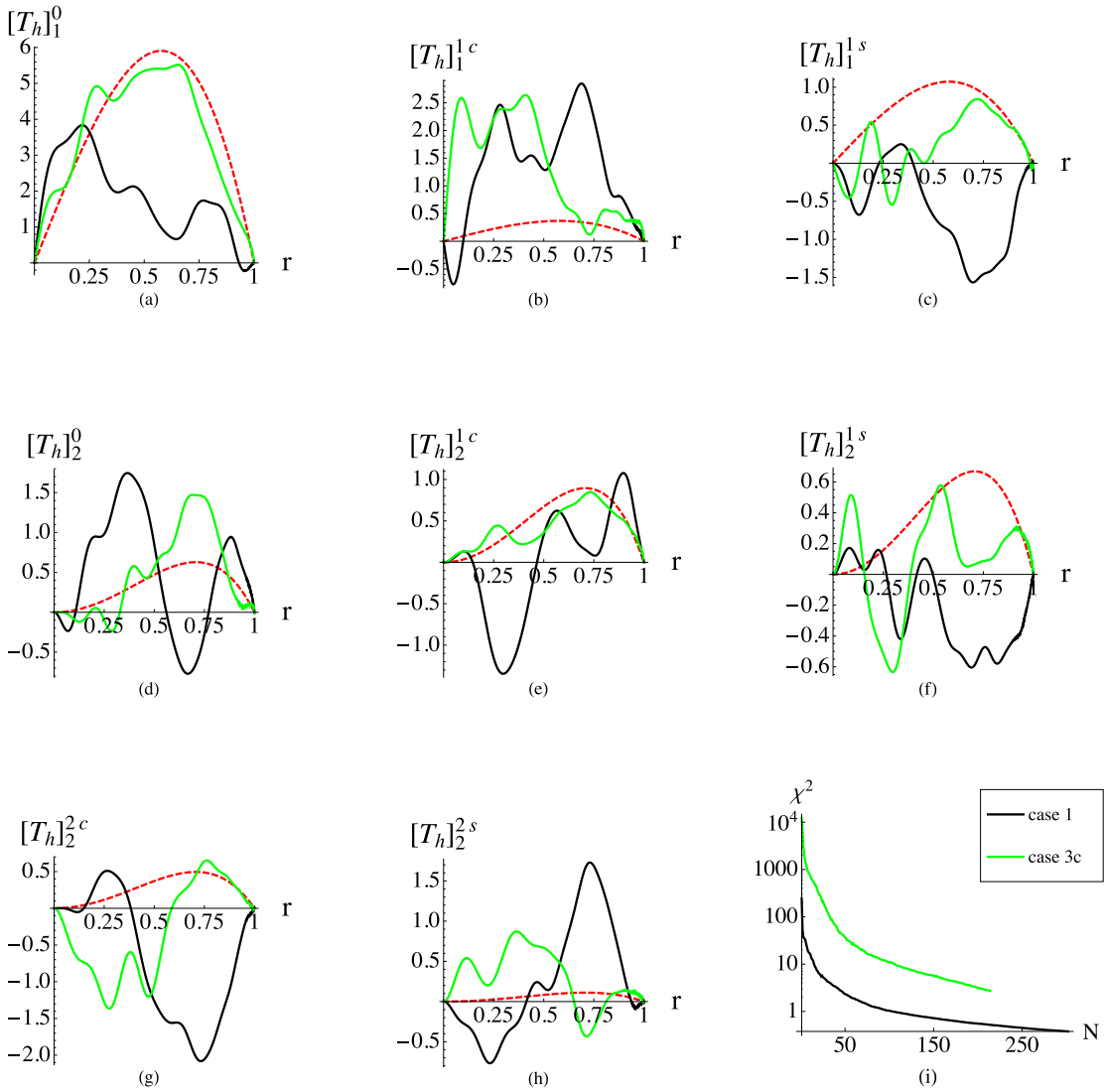

Figure 13. The toroidal part of the retrieved I.C. and the reduction of the misfit as a function of iteration for Cases 1 and 3c at the final iteration of each one for each spherical harmonic degree, l, and order m, where the dashed red lines stand for the truth and the solid lines are for the retrieved components (see the legend for the colour correspondence to different cases).

of $r = 0.85$, where, at later times, its magnitude is the greatest (Fig. 7c–d).

(iii) Case 3: observing B_r only at a location far away from the boundary.

In order to test the hypothesis that inductive processes will be favourable to a data assimilation scheme, we observe B_r at $r = 1/2$, a location at which the induction processes are strongest (Fig. 8). We also investigate the effect of the driving $\mathcal{F}$, the length of time window τ and the starting guess for $\mathbf{B}_0$.

We illustrate the method by considering the largest scale poloidal mode, described by the coefficient a_1. Fig. 9 illustrates the inner workings of the adjoint scheme at the third iteration of Case 1, where the adjoint poloidal mode for $a_1^\dagger$ starts from zero at the terminal time, $t = \tau$, backward propagates in time reaching, at $t = 0$, its initial value $a_1^\dagger(t = 0)$ with the value approximately 6, describing the downhill direction of χ^2 with respect to $a_1(t = 0)$. Fig. 9(b) is a close-up of the red rectangular region of Fig. 9(a), where the periodic jumps in $a_1^\dagger$ are due to the injection of the observed data into the adjoint field.

6.2 Results

Figs 10–13 show the retrieved initial state from the closed-loop assimilations compared with the true model, where we plot the individual spherical harmonic contributions to the radial component of the poloidal magnetic field, that is $[S_r]_l^m = \sum_n \frac{l(l+1)a_{(n,l,m)}\Phi_n^l(r)}{r^2}$, and the spherical harmonic contributions to the horizontal, that is $[T_h]_l^m = \sum_n \frac{b_{(n,l,m)}\Psi_n^l(r)}{r}$, for each spherical harmonic degree, l, and order, m. In all cases, the value of χ^2 decreases with iteration count, indicating the success of the methodology. Figs 10–11 illustrate the results from the most successful observational strategies, namely Cases 2, 3a and 3b. It is clear that the incorporation of velocity information leads to successful recovery, as does the observation of radial magnetic field deep in the core, as long as a reasonable starting guess is provided. We comment on the relationship of these types of data to the geophysical reality in the next section. Of particular note is the fact that we are able to recover large scale features of the toroidal magnetic field, despite the fact that they are not directly constrained by observation. For example, Fig. 11(a) shows excellent

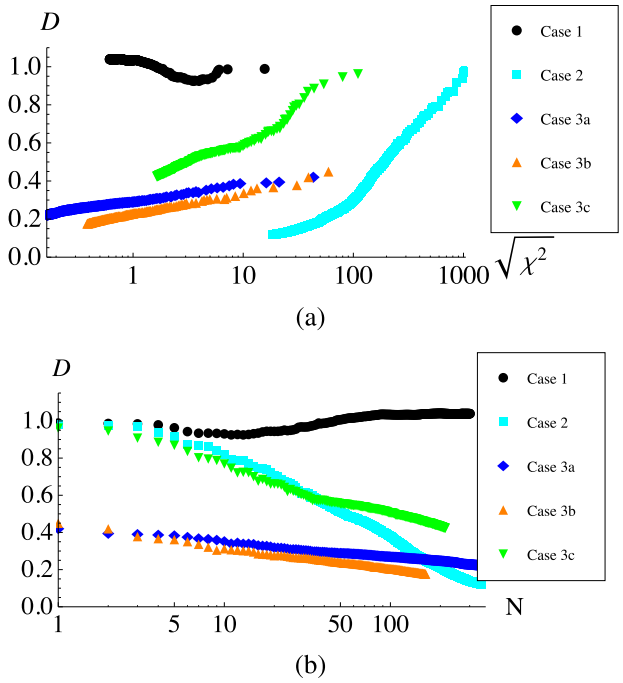

Figure 14. The reduction of D, defined by (35), as a function of $\sqrt{\chi^2}$ in (a) and number of iterations N in (b) on a log-linear scale for all test cases.

recovery of the largest scale toroidal mode. This illustrates the power of the data assimilation technique: the dynamic model gives access to properties of the system that are otherwise hidden. It is clear that Case 2 gives the best recovery of the initial field, based on the value of D (see Table 2), even when the starting guess $\mathbf{B}_0 = 0$ represents complete ignorance of the correct answer.

Figs 12 and 13 illustrate less successful observation strategies. Case 1, with observations at the CMB, where the fluid is quiescent (by dint of the no-slip B.C.), fails to recover the structure of the interior magnetic field, despite a rapid initial decrease in χ^2. Case 3c retrieves the structure of S_1^0 and T_1^0, which, since they together comprise 90 per cent of the energy of the dynamic system, define the large-scale evolution of the system. This test case also reveals one important aspect of the retrievability of the 4DVar scheme, that is the modes contributing less energy have a less significant contribution to the misfit. The misfit is less sensitive with respect to these parts of the unknown $\mathbf{B}_0$ than those of dominant intensity, and they are therefore more difficult to restore.

All five models are compared in Fig. 14, which show the decrease in D as a function of $\sqrt{\chi^2}$ and iteration number N. Of particular note are the low values of D for Cases 2, 3a and 3b, achieved at the end of the closed-loop test, further highlighting their success. The faster decrease of D in Case 3b, compared to that of 3a, indicates that the inclusion of the driving force improves the convergence rate of the assimilation scheme.

7 DISCUSSION

In this paper, we studied the retrievability of the trajectory of a simplified geodynamo system and demonstrated our results in five representative numerical experiments. Two observational strategies were successful: (i) 2-D observations of the radial magnetic field B_r, taken in a region in which magnetic induction dominates diffusion and when using a reasonable starting guess; (ii) 2-D observations of B_r at the CMB and of the flow in regions where it is strong.

Observations of the geomagnetic field taken on or above the Earth's surface constrain the radial part of the magnetic field, B_r, on the CMB—and not within the core. Inside the Ekman boundary layer, in which the flow is almost quiescent, magnetic diffusion dominates magnetic induction and thus smooths the magnetic signal from inside the core. This effect explains the success of our assimilation strategy based on observing the magnetic field on $r = 1/2$, compared to that based on observing B_r on the CMB. The implementation of non-slip B.C.s has the effect of causing magnetic induction to be exactly zero at the CMB which, in our relatively viscous models (compared to the Earth), appears to prevent successful reconstruction of the core field. One possible strategy may be the use of stress-free B.C.s (Kuang *et al.* 2009, 2010), which weakens the effect of the boundary; this is one avenue we plan to pursue.

We propose one strategy that may enhance convergence of the system. Preliminary determination of the surface flow field at the CMB, admittedly under the frozen-flux approximation, can be beneficial when the estimates are used as data in conjunction with magnetic field observations. This may be beneficial as a scheme to accelerate convergence during early iterations. Since the assumptions required to determine the flow field are at variance with our underlying dynamic model, it is essential to ultimately abandon these observations in later iterations. We recognize that this technique is tantamount to using the same data twice, and emphasize that the idea is solely to improve initial convergence when starting from an initial guess that is far from the expected truth. We circumvent the question of how best to make the velocity estimates from the magnetic field and its secular variation, but note the success of an analogous study (Rau *et al.* 2000) in reconstructing a dynamo's true flow field.

The lack of obvious prior information on the state of the core, from which a reasonable starting guess can be constructed, remains an outstanding challenge. Knowledge gleaned from torsional oscillation studies (Gillet *et al.* 2010) is clearly pertinent, since it constrains the cylindrical component of magnetic field. However, the azimuthally averaged nature of these estimates allows considerable latitude in constructing a reasonable 3-D starting model. We remain optimistic that approaches along these lines will bear fruit.

There are two issues that require further analysis. In our study we have treated perfect error-free data, an assumption that never occurs in geophysical reality. Thus performance when data are incomplete and noisy remains outstanding. As with all inverse problems, we can only reasonably expect to recover the large scale features of the model, and even these will benefit from the inclusion of either prior information or spatial regularization. No such regularization has been implemented in our study, and the choice of such requires careful consideration.

A major finding of our study is the encouraging performance of the data assimilation system when the time window of observations is as small as one convective time. Since this timescale is of O(100) years in the Earth's core, it suggests that with 400 yr of data, described by the *gufm1* model, there is the very real possibility of interrogating interior structures in the core. Outstanding issues include the need to address the time-varying buoyancy force in a variational manner, an aspect that was necessarily simplified in the present work. Future assimilation systems need to work at much higher values of the magnetic Reynolds number, necessitating higher resolutions in the numerical scheme.

ACKNOWLEDGEMENTS

This work was partly funded by ERC grant 247303 'MFECE' to AJ, and by SNF grant 200020-143596. PWL acknowledges funding from NERC grant NE/G014043/1.

REFERENCES

Boyd, J.P., 2001. *Chebyshev and Fourier Spectral Methods,* 2nd edn, Dover.

Buffett, B.A., Mathews, P.M. & Herring, T.A., 2002. Modeling of nutation and precession: effects of electromagnetic coupling, *J. geophys. Res.,* **107,** ETG 5-1–ETG 5-14.

Bullard, E.C. & Gellman, H., 1954. Homogeneous dynamos and terrestrial magnetism, *Phil. Trans. R. Soc. Lond,* **247**(928), 213–278.

Canet, E., Fournier, A. & Jault, D., 2009. Forward and adjoint quasi-geostrophic models of the geomagnetic secular variation, *J. geophys. Res.,* **114,** B11101, doi:10.1029/2008JB006189.

Christensen, U.R., Lesur, V. & Wardinski, I., 2012. Timescales of geomagnetic secular acceleration in satellite field models and geodynamo models, *Geophys. J. Intern.,* **190**(1), 243–254.

Compo, G.P., Whitaker, J.S. & Sardeshmukh, P.D., 2006. Feasibility of a 100-year reanalysis using only surface pressure data, *Bull. Am. Meteorol. Soc.,* **87,** 175–190.

de Koker, N., Steinle-Neumann, G. & Vlček, V., 2012. Electrical resistivity and thermal conductivity of liquid fe alloys at high p and t, and heat flux in earths core, *Proc. Natl. Acad. Sci.,* **109**(11), 4070–4073.

Donadini, F., Korte, M. & Constable, C.G., 2009. The geomagnetic field for 0–3ka: Part I. New data sets for high resolution global models, *Geochem. Geophys. Geosyst.,* **10,** Q06007, doi:10.1029/2008gc002295.

Evensen, G., 2006. *Data Assimilation: The Ensemble Kalman Filter,* Springer.

Fournier, A., Eymin, C. & Alboussiere, T., 2007. A case for variational geomagnetic data assimilation: insights from a one-dimensional, nonlinear, and sparsely observed MHD system, *Nonlin. Process. Geophys.,* **14,** 163–180.

Fournier, A. *et al.*, 2010. An introduction to data assimilation and predictability in geomagnetism, *Space. Sci. Rev.,* **155,** 247–291.

Ghil, M., 1989. Meteorological data assimilation for oceanographers, Part I: description and theoretical framework, *Dyn. Atmos. Oceans,* **13**(3–4), 171–218.

Gillet, N., Jault, D., Canet, E. & Fournier, A., 2010. Fast torsional waves and strong magnetic field within the Earth's core, *Nature,* **465,** 74–77.

Glatzmaier, G.A. & Roberts, P.H., 1995. A three-dimensional convective dynamo solution with rotating and finitely conducting inner core and mantle, *Phys. Earth planet. Inter.,* **91,** 63–75.

Jackson, A. & Finlay, C.C., 2007. Geomagnetic secular variation and its applications to the core, in *Treatise on Geophysics,* pp. 147–193, ed. Schubert, G., Elsevier.

Jackson, A., Jonkers, A.R.T. & Walker, R.M., 2000. Four centuries of geomagnetic secular variation from historical records, *Phil. Trans. R. Soc. Lond., A,* **358,** 957–990.

Jonkers, A.R.T., Jackson, A. & Murray, A., 2003. Four centuries of geomagnetic data from historical records, *Rev. Geophys.,* **41**(2), doi:10.1029/2002RG000115.

Kageyama, A. & Sato, T., 1995. Computer simulation of a magnetohydrodynamic dynamo. II, *Phys. Plasmas,* **2**(5), 1421.

Korte, M., Genevey, A., Constable, C.G., Frank, U. & Schnepp, E., 2005. Continuous geomagnetic field models for the past 7 millennia: 1. A new global data compilation, *Geochem. Geophys. Geosyst.,* **6,** Q02H15, doi:10.1029/2004GC000801.

Kuang, W., Tangborn, A., Wei, Z. & Sabaka, T., 2009. Constraining a numerical geodynamo model with 100 years of surface observations, *Geophys. J. Int.,* **179,** 1458–1468.

Kuang, W., Wei, Z., Holme, R. & Tangborn, A., 2010. Prediction of geomagnetic field with data assimilation: a candidate secular variation model for IGRF-11, *Earth, Planets Space,* **62,** 775–785.

Langel, R.A. & Estes, R.H., 1982. A geomagnetic field spectrum, *Geophys. Res. Lett.,* **9,** 250–253.

Li, K., Jackson, A. & Livermore, P.W., 2011. Variational data assimilation for the initial value dynamo problem, *Phys. Rev. E,* **84,** doi:10.1103/PhysRevE.84.056321.

Li, K., Livermore, P.W. & Jackson, A., 2010. An optimal Galerkin scheme to solve the kinematic dynamo eigenvalue problem in a full sphere, *J. Comp. Phys.,* **229,** 8666–8683.

Liu, D., Tangborn, A. & Kuang, W., 2007. Observing system simulation experiments in geomagnetic data assimilation, *J. geophys. Res.,* **112,** B08103, doi:10.1029/2006JB004691.

Livermore, P.W., 2010. Galerkin orthogonal polynomials, *J. Comput. Phys.,* **229,** 2046–2060.

Lynch, P., 2008. The origins of computer weather prediction and climate modeling, *J. Comput. Phys.,* **227**(7), 3431–3444.

Nocedal, J., 1980. Updating quasi-Newton matrices with limited storage, *Math. Comput.,* **35,** 773–782.

Nocedal, J. & Wright, S.J., 2006. *Numerical Optimization,* 2nd edn, Springer.

Olsen, N., Mandea, M., Sabaka, T. & Tøffner-Clausen, L., 2009. CHAOS-2—a geomagnetic field model derived from one decade of continuous satellite data, *Geophys. J. Int.,* **179**(3), 1477–1487.

Olson, P., 2007. Overview, in *Treatise of Geophysics,* Vol. 8, pp. 1–30, ed. Olson, P., Elsevier.

Rau, S., Christensen, U.R., Jackson, A. & Wicht, J., 2000. Core flow inversion tested with numerical dynamo models, *Geophys. J. Int.,* **141,** 485–497.

Siscoe, G. & Solomon, S.C., 2006. Aspects of data assimilation peculiar to space weather forecasting, *Space Weather,* **4**(4), doi:10.1029/2005SW000205.

Sun, Z., Tangborn, A. & Kuang, W., 2007. Data assimilation in a sparsely observed one-dimensional modeled MHD system, *Nonlin. Process. Geophys,* **14,** 181–192.

Talagrand, O., 2010. Variational assimilation, in *Data Assimilation: Making Sense of Observations,* pp. 41–67, eds Lahoz, W., Khattatov, B. & Menard, R., Springer.

Tarantola, A., 1984. Inversion of seismic reflection data in the acoustic approximation, *Geophysics,* **49**(8), 1259–1266.

Zhang, K.K., 1991. Convection in a rapidly rotating spherical shell at infinite prandtl number: steadily drifting rolls, *Phys. Earth planet. Inter.,* **68**(1–2), 156–169.

APPENDIX A: A SYNTHETIC MAGNETIC PROFILE

Using the following assumptions, we create a 3-D, synthetic model of magnetic field inside the core. We use a variety of geophysical constraints reported in the literature in its construction. We assume that

A.1. B_r^* matches the *gufm1* model at the CMB in 1990 for each $l, m \leq 2$.

A.2. The horizontal rms of B_r^* at radius $r_i = \frac{7}{20}$ is 4.6 mT (Buffett *et al.* 2002).

A.3. For each l and m, the radial magnetic field at $r = r_i$ is proportional to the field at the CMB.

A.4. There is equipartition of energy in the magnetic field between its poloidal and toroidal components for each l and m.

A.5. Only the lowest order radial mode contributes to the toroidal field.

Denoting $(\overline{B_r})_{(l,m)}(r)$ as the non-dimensionalized horizontal rms of B_r as a function of the radius r for the spherical harmonic degree, l, and order, m, defined as

$$(\overline{B_r})_{(l,m)} = \sqrt{\frac{\left[l(l+1)S_l^m\right]^2}{4\pi r^4}}, \tag{A1}$$

we have that the radial magnetic field satisfies

$$(\overline{B_r})_{(l,m)}(r_i) = \gamma \sqrt{\frac{(\overline{B_r})^2_{(l,m)}(1)}{\sum_{l,m}(\overline{B_r})^2_{(l,m)}(1)}}, \tag{A2}$$

where γ is the non-dimensionalized value of B_r at $r_i = \frac{7}{20}$. Together with assumption A.1 and eqs (A1) and (A2), one determines the poloidal scalars for each l and m at $r = 1$ and $r = 7/20$, that is

$$\frac{l(l+1)S_l^m(r_i)}{\sqrt{4\pi}r_i^2} = \gamma \sqrt{\frac{(\overline{B_r})^2_{(l,m)}(1)}{\sum_{l,m}(\overline{B_r})^2_{(l,m)}(1)}} \quad \text{and}$$

$$\frac{l(l+1)S_l^m(1)}{\sqrt{4\pi}} = (\overline{B_r})_{(l,m)}(1). \tag{A3}$$

The poloidal scalar $S_l^m(r)$ can be further represented by the radial basis functions as $S_l^m(r) = a_1\Phi_1^l(r) + a_2\Phi_2^l(r)$. For each l and m, the coefficients a_1 and a_2 can be uniquely determined by eq. (A3).

For the toroidal field, we assume a simple radial profile of the toroidal basis function of degree $n = 1$, $T_l^m = b_1\Psi_1^l$, and match the energy with the poloidal part for each l and m, that is $b_1 = \sqrt{a_1^2 + a_2^2}$.